Advances in
Geo-Energy Research

Vol. 19, No. 1, p. 82-96, 2026

Original article

Evolution of pore-fracture system across different maturity levels and its implications for carbon dioxide sequestration in lacustrine shale

Xin Tian[1], Zhejun Pan[1], Yeping Ji[2], Mehdi Ostadhassan[1,3], Bo Liu[1], Mengdi Sun[1,4]*

[1]*National Key Laboratory of Continental Shale Oil, Northeast Petroleum University, Daqing 163318, P. R. China*
[2]*Commonwealth Scientific and Industrial Research Organisation, Perth, WA 6151, Australia*
[3]*Institute of Geosciences, Marine and Land Geomechanics and Geotectonics, Christian-Albrechts-Universität, Kiel 24118, Germany*
[4]*Heilongjiang Provincial Key Laboratory of Continental Shale Oil, Daqing 163712, P. R. China*

Keywords:
Pore-fracture connectivity
maturation gradient
fractal dimension
neutron scattering
carbon dioxide storage

Cited as:
Tian, X., Pan, Z., Ji, Y., Ostadhassan, M., Liu, B., Sun, M. Evolution of pore-fracture system across different maturity levels and its implications for carbon dioxide sequestration in lacustrine shale. Advances in Geo-Energy Research, 2026, 19(1): 82-96.
https://doi.org/10.46690/ager.2026.01.07

Abstract:
The geometry and topology of shale pore-fracture systems govern hydrocarbon migration and control the feasibility of geological carbon dioxide storage in shale reservoirs. This study examines lacustrine shale across a range of maturities by integrating (ultra) small-angle neutron scattering, repeated mercury intrusion capillary pressure, field-emission scanning electron microscopy, and computed tomography following Wood's metal impregnation. The pore system is divided into four pore-size classes, and their volumes and connectivity are tracked with increasing thermal maturity. At low maturity, mechanical compaction and early cementation reduce the total pore volume and concentrate connected porosity in fractures. As maturity increases, newly formed organic-matter pores lead to a modest increase in total pore volume, while liquid hydrocarbons generated within the oil window occupy part of the pore space and weaken pore-fracture connectivity. At high maturity, the secondary cracking of liquid hydrocarbons to gas raises pore pressure, partially reopens previously sealed pores and fractures, and enhances both total pore volume and pore-fracture connectivity. These results indicate that mature to high-mature lacustrine shales provide more pore surface area, storage space, and connected pathways for the long-term storage of carbon dioxide than low-maturity shales.

---

1. Introduction

Lacustrine organic-rich shale commonly contains pervasive bedding-parallel fractures (Sun et al., 2021). This shale is characterized by an organic-inorganic dual-reservoir architecture, in which both the shale matrix and fracture networks provide storage space for shale oil (Sun et al., 2021; Hua et al., 2022). Compared with the Eagle Ford shale oil system that has achieved large-scale commercial development in North America, lacustrine shale oil in China is generally less mobile, where the produced hydrocarbons are often dominated by condensate to light crude oil (Jarvie, 2017). Recent geochemical evidence further indicates that lacustrine shale can exhibit high total organic carbon (TOC) and is primarily composed of type I kerogen (Zhao et al., 2020). These lacustrine shales span a broad maturity range, and their pore structure is inherently heterogeneous. The maturity variability and structural complexity jointly create challenges for both shale oil development and carbon dioxide (CO_2) storage. Therefore, clarifying the pore-fracture system of lacustrine shale is essential.

Extensive research has examined the factors controlling

Yandy Scientific Press

---

*Corresponding author.
E-mail address: 228001010018@stu.nepu.edu.cn (X. Tian); zhejun.pan@nepu.edu.cn (Z. Pan); tim.yeping@gmail.com (Y. Ji); mehdi.ostadhassan@gmail.com (M. Ostadhassan); liubo@nepu.edu.cn (B. Liu); sunmd@nepu.edu.cn (M. Sun).

Received November 16, 2025; revised December 15, 2025; accepted January 9, 2026; available online January 12, 2026.

shale pore structure, with thermal maturity, mineral composition and organic-matter characteristics commonly recognized as key drivers (Wei et al., 2019). Among these, thermal maturity is widely regarded as the most influential factor affecting shale pore structure (Wei et al., 2019). Jarvie (2007) linked shale pore structure to vitrinite reflectance (R_o) and suggested that porosity can increase as kerogen converts to petroleum. However, investigations of the Barnett Shale reported that the porosity-maturity relation is not strictly linear, implying a more complex evolutionary pathway (Loucks et al., 2012). Mastalerz et al. (2013) characterized the pore structures of marine New Albany shale samples spanning R_o from 0.35% to 1.41% and proposed a systematic model for pore structure evolution. However, this model may not be applicable to the pore structure evolution of lacustrine shale.

The R_o has been used widely as an indicator of thermal maturity, and its influence on shale pore evolution has been evaluated using a range of approaches, including adsorption (Liu et al., 2017, 2023), mercury injection capillary pressure (MICP), (ultra-) small-angle neutron scattering ((U)SANS), field-emission scanning electron microscopy (FE-SEM), computed tomography (CT), nuclear magnetic resonance, and atomic force microscopy. According to the IUPAC convention, shale pores are commonly grouped into micropores (< 2 nm), mesopores (2-50 nm), and macropores (> 50 nm). While this classification has been broadly adopted, it is most suitable for materials dominated by nano-sized pores and containing few fractures (Li et al., 2016).

Given the limited applicability of the IUPAC classification for lacustrine shale that is characterized by the abundance of nanometer-sized pores and micrometer-sized fractures, there is a pressing need to redefine the classification for pore space in a pore-fracture system, as it would enable us to understand the dynamics of pore evolution in shale formations as the thermal maturity advances. In continental shales, several classification schemes have been proposed on the basis of lithofacies, OM type and maturity, and dominant pore types, and some of these schemes have been widely applied in shale oil exploration (Wen et al., 2025). These schemes primarily focus on facies and hydrocarbon enrichment. In this study, lacustrine shales are classified according to the relative existence of micropores, mesopores, macropores, and fractures, as well as their connectivity along the maturity sequence, as captured by MICP, (U)SANS and WM imaging. This pore-fracture-based classification is closely linked to storage and sealing properties and can complement existing lithofacies-based schemes in practical reservoir evaluation.

This study aims to elucidate how the pore-fracture system evolves across the lacustrine shale maturity sequence as well as to evaluate its CO_2 storage capacity by integrating advanced experiments, including (U)SANS, repeated mercury intrusion capillary pressure (repeated-MICP), and imaging techniques (FE-SEM and CT scanning) on Wood's metal (WM)-impregnated samples. The experimental samples, retrieved from lacustrine shale in the Songliao Basin, Northeast China, cover a range of thermal maturities. First, the pore-fracture system is categorized by quantifying the fractal features derived from the MICP curves. Then, (U)SANS and FE-SEM observations of WM-impregnated samples are employed to establish a model for the evolution of the pore-fracture system. Finally, pore-fracture connectivity in the lacustrine shale samples is delineated through repeated-MICP and CT scanning after WM impregnation. This integrated approach facilitates the assessment of CO_2 storage potential in shales at different maturity levels and provides insights for optimizing future field operations.

2. Materials and Methods

2.1 Lacustrine shale samples

Six lacustrine shale specimens spanning a thermal-maturity interval of R_o 0.58%-1.52% were obtained from the first member of the Upper Cretaceous Qingshankou Formation (Fig. S1). The R_o and TOC were measured using an MPV-3 microphotometer 806 apparatus and a LECO CS230 carbon analyzer, respectively. As reported in Table S1, these specimens are organic-rich, with TOC values of 1.76-5.13 wt.%. For mineralogical determination, powdered aliquots (200 mesh) were subjected to X-ray diffraction (XRD) analysis (Table S1). The six specimens show broadly comparable lithofacies, mineral assemblages, and TOC contents, thereby minimizing lithological differences among maturity levels. Because each maturity stage is represented by a single core plug, the dataset is interpreted as a representative maturity sequence rather than a statistical population.

2.2 Methods

2.2.1 MICP test

MICP measurements were conducted using a Micromeritics AutoPore IV 9620 porosimeter. Mercury pressure was ramped from 0.3 to 60,000 psia, and the equilibration time at each pressure step was fixed at 30 s. The MICP-derived pore-size distribution was computed using the Washburn equation over an effective pore-size range of ~ 3 nm to 780 μm. The shale samples were cut into 1 cm^3 cubes for the MICP tests, with each face polished to minimize pockmark effects. Subsequently, the shale samples were dried at 80 °C for 24 h. To separate the cumulative intrusion volume from the residual mercury volume distribution, repeated-MICP measurements were performed on the same set of samples (Zhao et al., 2023). According to the Washburn equation, the maximum pressure used in this study corresponds to a minimum pore-throat diameter of approximately 3-4 nm. Accordingly, MICP was primarily applied to characterize pore throats larger than ~ 3-4 nm. MICP was mainly utilized to characterize pore throats larger than this limit and to evaluate pore-throat connectivity and related fractal properties, whereas smaller nanopores and the total nanopore volume were constrained using (U)SANS measurements.

2.2.2 Neutron scattering experiment

SANS and USANS measurements were conducted using the QUOKKA and KOOKABURRA instruments at the Australian Centre for Neutron Scattering, operated by the Australian Nuclear Science and Technology Organization

(ANSTO), respectively. Representative shale wafers were sliced into $10 \times 10 \times 0.5$ mm^3 specimens, which were then sealed in quartz cells with deionized water to minimize water loss and maintain sample conditions. For SANS, the scattering vector (Q) range was 0.006-0.65 Å^{-1}, corresponding to pore sizes of 10-1,000 nm, with neutron wavelengths of 20 m and 4 m. For USANS, to improve statistics given the weak scattering of shale, a longer acquisition time was used; the probed size range was 100 nm to 20 μm after combining SANS and (U)SANS.

Following the empirical relationship proposed by Sun et al. (2020), the shale pore-fracture system could be approximated as a polydisperse spherical pore network, with the relationship between Q and pore radius (R) given by $R \approx 2.5/Q$. Therefore, the Q range of the SANS/(U)SANS corresponds to a pore radius range from ~ 0.5 nm to 10 μm. In addition, the SLD of each shale sample was calculated by a volumetric averaging of SLD values of each shale component (Table S1). Finally, the pore structure information of the samples was calculated by following the polydisperse size distribution model (PDSM).

2.2.3 WM impregnation and FE-SEM imaging

Shale specimens were prepared as 1 cm^3 cubes, polished on all faces, and oven-dried at > 80 °C for more than 48 h. Next, WM impregnation was carried out using a custom high-pressure apparatus. Samples were evacuated and heated to 110 °C for 30 min to fully melt the WM (melting point: 80 °C). Injection pressure was applied and increased stepwise, with a maximum pressure of 200 MPa, and the cell was then cooled to ~ 20 °C to solidify the injected metal. Impregnated specimens were sectioned perpendicular to bedding, and 2D pore-structure images were acquired by FE-SEM (Zeiss Supra55) at 20 kV. On the basis of the combined observations, WM-filled features were used to identify connected pore-fracture pathways at the applied pressure.

To minimize artificial modification of the pore system, the injection pressure was increased stepwise and the maximum pressure of 200 MPa was selected to remain well below the typical uniaxial compressive strength reported for lacustrine shales (Wang et al., 2021b). For representative samples, micro-CT and FE-SEM observations obtained before and after WM impregnation did not reveal newly formed fractures or an obvious widening of pre-existing fractures. The WM-filling patterns were also consistent with the pore-fracture characteristics inferred from the MICP and (U)SANS results, suggesting that the applied pressure did not significantly alter the original pore structure and that WM predominantly highlights pre-existing connected pore-fracture pathways.

2.2.4 Synchrotron radiation micro-CT and 3D reconstruction

CT scanning was conducted using synchrotron radiation micro-CT at the Beijing Synchrotron Radiation Laboratory, with a pixel size resolution of 1 μm. The energy of the storage ring was operated at 20 KeV, magnification of 10×, and the equilibration time (acquired the time between two projected images) was set at 6 s. In this study, WM-impregnated shale samples were prepared as 1 mm diameter plugs. Shale samples were securely mounted on the stage and rotated in 0.125° increments over a total of 180°. Prior to scanning, ten darkfield images were acquired to correct for intensity variations. From each sample, 1,440 projection images were acquired and analyzed using HEPSCT software according to the following steps: (1) Load darkfield and projection images; (2) preprocess images by applying denoising, background subtraction, negative cutoff, and background normalization; and (3) reconstruct data using the filtered back-projection algorithm. Fig. S2(a) depicts the original image from shale sample A, while the grayscale-adjusted images in Fig. S2(b) illustrate the spaces between pores, the matrix, mineral particles, and the WM. Noise was next eliminated from the image using the median filter function to improve image quality (Fig. S2(c)). Subsequently, threshold segmentation was performed (Fig. S2(d)), and the three-dimensional (3D) structure of the shale samples was reconstructed using AVIZO software, highlighting the skeletal structure and WM-impregnated pores (Fig. S2(e)). To ensure accuracy, the digital core pore structure was refined by adjusting the threshold separation values until the digital core porosity aligned with the MICP-porosity.

3. Results

3.1 MICP tests

3.1.1 Characterization and classification of the pore-fracture system

To quantify the multi-scale pore-throat structure and obtain the key pore-structure parameters for subsequent analyses, MICP measurements were conducted on the six shale samples. As illustrated in Fig. S3(a), the cumulative intrusions of mercury in six shale samples increases. The intrusion volume rises rapidly at lower pressure (< 100 psia) and higher pressure (10,000 psia), while it grows more gradually in the medium pressure range (100-10,000 psia), suggesting the presence of both nano- and micro-size pore spaces. In addition, hysteresis is observed, denoting that approximately 65%-87% of mercury was retained in the pore spaces. Table 1 presents the pore structure parameters and bulk density obtained from MICP. Bulk density was calculated at the initial pressure, whereas porosity values were derived from cumulative intrusion at the maximum pressure. Pore-size distributions were calculated using the Washburn equation (Sun et al., 2022; Wen et al., 2023), which showed that pores in the 3-30 nm range contribute more than half of the TPV (Fig. S3(b)). In addition, micron sized pores (> 10 μm) are prominent.

The mercury saturation curve provides information on pore throats and their associated pore-space structure. To further differentiate pore-throat regimes, we applied fractal analysis to the intrusion data. Because self-similar pore geometries often exhibit comparable fractal dimensions, the fractal dimension derived from a log-log fit can be used to diagnose structural similarity. Here, fractal segments are identified by fitting linear relationships with high goodness-of-fit ($R^2 > 0.98$) over distinct saturation ranges (Sun et al., 2020). Accordingly, the fractal characteristics of the pore system were obtained from

Table 1. Pore structure parameters obtained from MICP and repeated-MICP analyses.

Sample	Bulk density (g/cm^3)	MICP				Repeated-MICP			
		Porosity (%)	TPV (cm^3/g)	TPA (m^2/g)	APTD (nm)	Porosity (%)	TPV (cm^3/g)	TPA (m^2/g)	APTD (nm)
A	2.25	9.36	0.054	6.59	13.62	4.39	0.019	4.61	9.51
B	2.27	5.13	0.023	4.84	11.14	2.86	0.012	3.28	9.35
C	2.18	6.08	0.023	3.55	12.92	3.85	0.012	1.98	12.42
D	2.22	4.67	0.022	8.81	8.01	3.02	0.013	4.84	9.61
E	2.15	6.82	0.035	12.40	8.11	4.44	0.019	2.97	9.41
F	2.52	8.69	0.042	17.42	9.18	5.88	0.027	1.99	9.78

Notes: TPV represents total pore volume; TPA represents total pore area; and APtD is average pore-throat diameter.

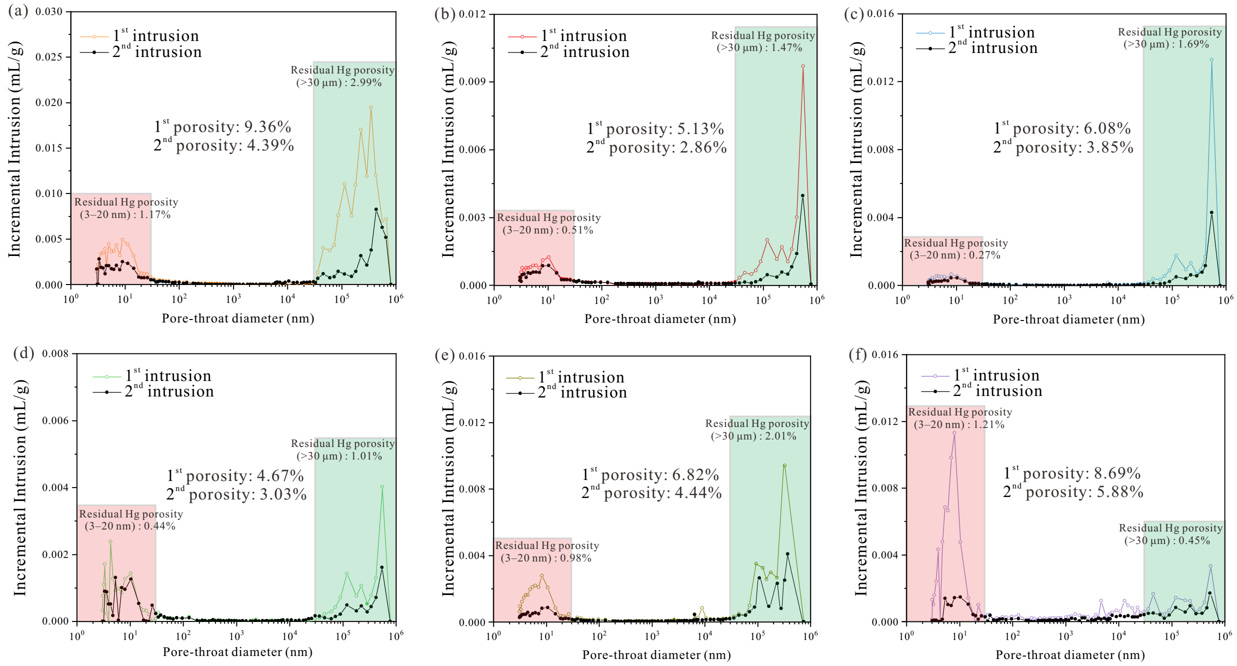

Fig. 1. Pore volume distribution versus pore-throat diameters of original and re-intrusion samples from repeat-MICP of six shale samples: (a) Sample A, (b) Sample B, (c) Sample C, (d) Sample D, (e) Sample E, and (e) Sample F.

the MICP data based on the following equation:

$$S_{Hg} = 1 - \left(\frac{p_c}{p_{c,\min}}\right)^{\bar{D}-3} \tag{1}$$

From Eq. (1), we can obtain:

$$\lg(1 - S_{Hg}) = (\bar{D}-3)\lg p_c - (\bar{D}-3)\lg p_{c,\min} \tag{2}$$

where $\bar{D}$ denotes the fractal dimension; P_c denotes the capillary pressure; S_{Hg} denotes the mercury saturation in pores at mercury intrusion pressure P_c; and $P_{c,\min}$ is the minimum capillary pressure.

The fractal characterization curves (Fig. S3(c)) for the shale pore-fracture system were derived from the mercury saturation curve obtained by MICP (Fig. S3(d)). Four linear intervals can be distinguished on the fractal characterization curves (Fig. S3(c)). Using fractal-dimension analysis, three "inflection points" were identified on the intrusion mercury saturation curve (Fig. S3(c)), corresponding to pressures of $P_1 = 1.48$ MPa, $P_2 = 12.24$ MPa, and $P_3 = 61.15$ MPa, with associated pore-throat diameters of 800 nm, 100 nm, and 20 nm, respectively. On the basis of the locations of these inflection points, the pore-throat system of shale was partitioned into micropore-throats (< 20 nm), mesopore-throats (20-100 nm), macropore-throats (100-800 nm), and fractures (> 800 nm).

3.1.2 Repeated MICP measurements

The repeated-MICP measurements were performed on the same specimens to quantify residual mercury and its distribution after the first intrusion-extrusion cycle. Fig. 1 presents the pore volume distributions within the pore-throat diameter range of 3-780 μm for both the initial and repeated intrusion. In the repeated-MICP curves, the incremental intrusion volume

Table 2. Measurement of the physical parameters of shale samples by (U)SANS.

Sample	R_o (%)	Porosity (%)	MPD (nm)	APD (nm)	SSA (m^3/g)	NDP (10^{18} $1/cm^3$)
A	0.58	7.41	150.9	1,140	22.73	6.42
B	0.73	7.23	114.1	1,190	21.08	5.54
C	0.86	7.62	106.1	1,083	17.39	6.18
D	0.98	4.15	82.5	1,005	24.03	6.48
E	1.32	4.61	88.8	1,009	21.99	7.21
F	1.52	5.51	98.2	1,053	26.93	7.96

Notes: MPD represent median pore diameter; APD denotes average pore diameter; and SSA is specific surface area.

is reduced relative to the initial run because some pore space remains occupied by residual mercury. Residual mercury is primarily retained in pores larger than 30 μm in most samples. Across the six samples, residual mercury porosity in the 3-30 nm range is 4.47%-14.36%, whereas in pores larger than 30 μm, it ranges from 5.17% to 31.94%.

3.2 (U)SANS measurements

(U)SANS/SANS measurements were performed to quantify the pore structure of the shale samples across the nano- to the micron-scales. Figs. S4(a), S4(c), S4(e), S4(g), S4(i), and S4(k) display the combined (U)SANS and SANS raw scattering profiles from each shale sample. The workflow of (U)SANS data processing was as follows: (1) the USANS data was desmeared using Lake's algorithm, and the SANS and (U)SANS data were combined to obtain the final $1-\bar{D}$ scattering curve (Figs. S4(a), S4(c), S4(e), S4(g), S4(i), and S4(k)); (2) the flat background scattering intensity of shale samples was obtained by calculating the slope of the $Q^4I(Q)$ vs. Q^4 plot, then subtracted from the combined USANS and SANS intensity profile (Fig. S5(a) and Figs. S4(b), S4(d), S4(f), S4(h), S4(j), and S4(l)). Following the Porod invariant (PI) method, the relationship between porosity and $I(Q)$ can be expressed as below when the shale is approximated as a two-phase system:

$$\int_0^{\infty} Q^2 I(Q)\mathrm{d}Q = 2\pi^2(\rho_1-\rho_2)^2\varphi(1-\varphi) \tag{3}$$

where Q is the scattering vector; $I(Q)$ is the scattering intensity; ρ_1 is the SLD of the shale solid; ρ_2 is the SLD of the pore space; φ is the porosity.

The (U)SANS data were processed using the PDSM, and the non-negative least-squares fitting method implemented in the Irena-macros software was adopted. The pore-structure parameters derived from (U)SANS are summarized in Table 2. In general, shale samples with relatively low thermal maturity ($R_o < 0.9\%$; A-C) exhibit markedly higher porosity, median pore diameter, and average pore diameter (APD) than the higher-maturity samples (D-F). The mean specific surface area (SSA) of the six shale samples is 22.35 m^2/g, ranging from 17.39 to 26.93 m^2/g. In addition, the number density of pores (NDP), which quantifies the abundance of pores in the sample, was calculated, and the results indicate that samples with $R_o > 0.9\%$ tend to have greater NDP. The pore size distribution for all shale samples obtained from (U)SANS tests is depicted in Fig. S5(b). The pore volume of the shale samples is characterized by micropores (< 20 nm), mesopores (20-100 nm), macropores (100-800 nm), and fractures (> 800 nm), indicated by three major peaks in the PSD curves at 1-5 nm, 100-500 nm, and 1-4 μm, respectively.

The scattering intensity of each shale sample includes both accessible and inaccessible pores. In this study, micropores were defined as pores 1-20 nm in size, regardless of whether they are open or closed. The PDSM results indicate a single dominant volumetric peak at 1-4 nm, which contributes over 60% of the total micropore volume (Fig. S5(b)). Micropore porosity ranges from 1.34% to 2.76%, and micropore SSA ranges from 10.26 to 18.31 m^2/g (Table S2). Among the samples, F has the largest volume of micropores < 4 nm, whereas D has the smallest.

The mesopore volume accounts for $\sim 9.8\%$-11.7% of the TPV in each sample. Sample A has the largest mesopore volume, whereas sample D has the smallest. Overall, mesopores in the lacustrine shale show a unimodal distribution (Fig. S5(b)), with pores of ~ 60-70 nm contributing most of the mesopore volume and only few pores existing in the 12-36 nm range. The mesopore SSA varies from 1.97 to 3.76 m^2/g, with a mean value of 2.72 m^2/g (Table S2).

The macropore and fracture volumes of the lacustrine shale are similar, each contributing more than 30% of the TPV. Macropores are mainly 300-500 nm in size (Fig. S5(b)), and fractures are mainly 2-4 μm (Fig. S5(b)). The APD is 356.86 nm for macropores and 3.64 μm for fractures. Macropores are most developed in sample C, whereas fractures are most developed in sample B. The APD is 356.86 nm for macropores and 3.64 μm for fractures.

3.3 FE-SEM observation after WM impregnation

The six lacustrine shale specimens subjected to WM injection were inspected under SEM (Figs. 2 and 3). The bright areas represent fractures and sparse matrix pores filled with WM. The WM is visible in the fractures (Figs. 2(a) and 2(b)) and adjacent pores (Figs. 2(c) and 2(d)) of the low-maturity shale samples A and B, but it was not detected in pores

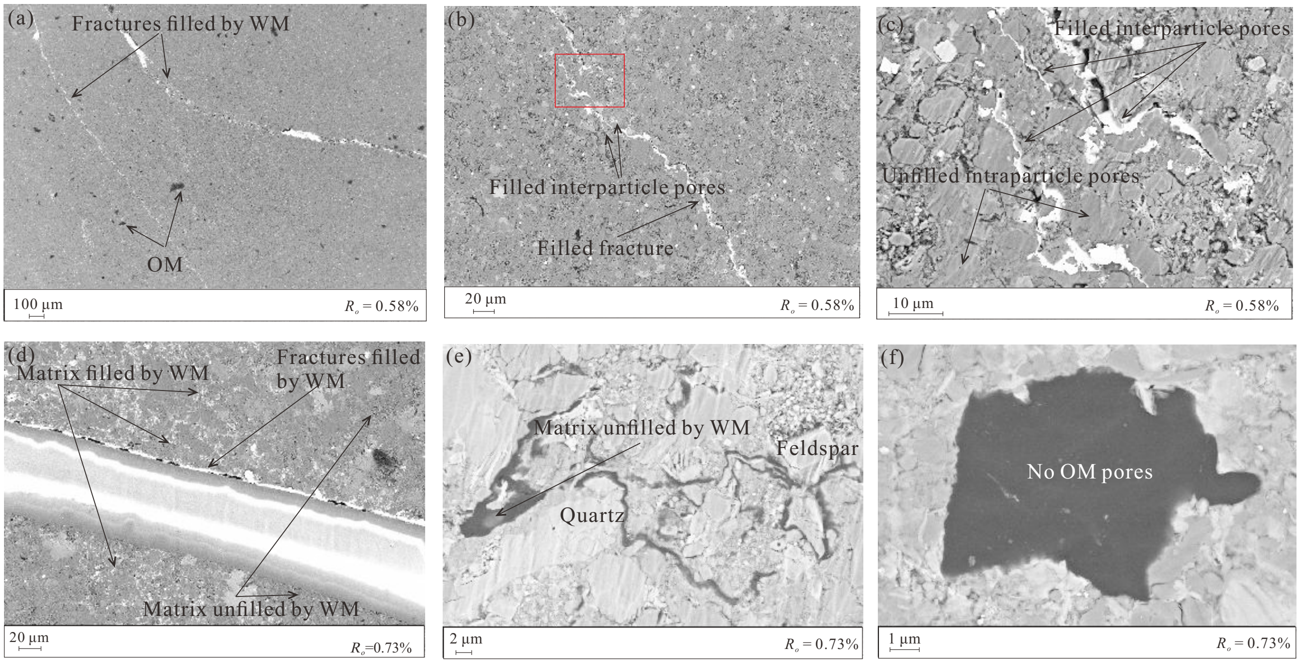

Fig. 2. FE-SEM images of low-maturity shale samples after WM impregnation, illustrating that WM preferentially fills fractures and a limited number of adjacent interparticle pores, while OM remains largely non-porous. (a) WM-filled fractures; (b)-(d) WM invading fractures and connected matrix pores but not reaching more distant pores; and (e)-(f) quartz and feldspar surrounding OM with no visible organic pores. (a)-(c) Sample A and (d)-(f) Sample B.

located farther from the larger fractures (Fig. 2(c)). In sample A, most interparticle pores linked to fractures are occupied by WM, but no WM was detected in pores surrounding the OM, indicating poor connectivity between OM and fractures. In contrast, the connectivity in sample B is markedly higher than that in sample A, where most connected intergranular pores are filled with WM, and WM was also observed in interparticle pores several hundred μm away from the fractures (Fig. 2(d)). Furthermore, no newly developed organic pores were observed in the low-maturity shale (Figs. 2(e) and 2(f)). Overall, FE-SEM imaging of the six WM-impregnated lacustrine shales indicated that at low maturity, WM mainly occurs in fractures and in a small number of matrix pores adjacent to these fractures (Fig. 2). This suggests that fluid pathways are predominantly controlled by fractures and that most matrix pores, including organic pores, are effectively connected to the fracture network.

The WM was able to enter the interparticle pores (Fig. 3(b)), clay mineral associated pores (Fig. 3(e)), and clay mineral associated fractures (Fig. 3(f)) via the fractures (Fig. 3(a)) in middle-mature and high-mature shale samples (C, D, E, and F). Moreover, WM was also observed within fractures at the margins of OM in mature shales (Fig. 3(g)), indicating substantially stronger pore connectivity in mature shale samples than in their low-maturity counterparts. The onset of OM pores can be observed in shale sample C at $R_o = 0.86\%$ (Fig. 3(c)); at this stage, WM fills the pore space surrounding the OM (Fig. 3(b)) but does not penetrate into the OM pores (Fig. 3(c)). It is worth noting that the WM is still not found in the organic pores of the highest-maturity shale sample, F, indicating that the pore throat within the organic pores is less than 7 nm (corresponding to the pore diameter at 200 MPa). In addition, dissolution pores were detected in the minerals surrounding the OM (Fig. 3(c)).

Overall, WM penetration into the lacustrine shale samples was limited, indicating generally poor pore connectivity. In most cases, fractures provided connections only to nearby matrix pores on the order of tens of μm, and WM did not access the majority of pore space within the shale matrix (Figs. 2(a) and 3(a)). In the most mature sample (F), OM-hosted pores extended from a few μm to several hundred μm (Fig. 3(h)), which is far larger than the minimum pore size accessible to WM at 200 MPa (i.e., ~4 nm at 154 MPa (Hu et al., 2015)). Consistent with these observations (Figs. 2 and 3), CT-based pore-network modeling yielded a low connected-porosity range of 1.27%-1.97%, supporting that only a minor portion of the matrix pore volume is effectively linked to the fracture network, even at the highest maturity.

3.4 CT Measurements after WM impregnation

Micro-CT imaging (Fig. 4) was used to map WM distribution and reconstruct the 3D connected network within the shale samples. Owing to its higher X-ray attenuation than the rock matrix, WM-filled fractures appear as bright features in 2D slices (Fig. 4(a)). WM impregnation further increases the grayscale contrast between connected and isolated pores, improving the reliability of connectivity assessment. Cylindrical sub-volumes (diameter 600 μm; height 1,000 μm) were extracted and analyzed at 1 μm resolution. WM occurs predominantly in microfractures, forming flaky, stratified mor-

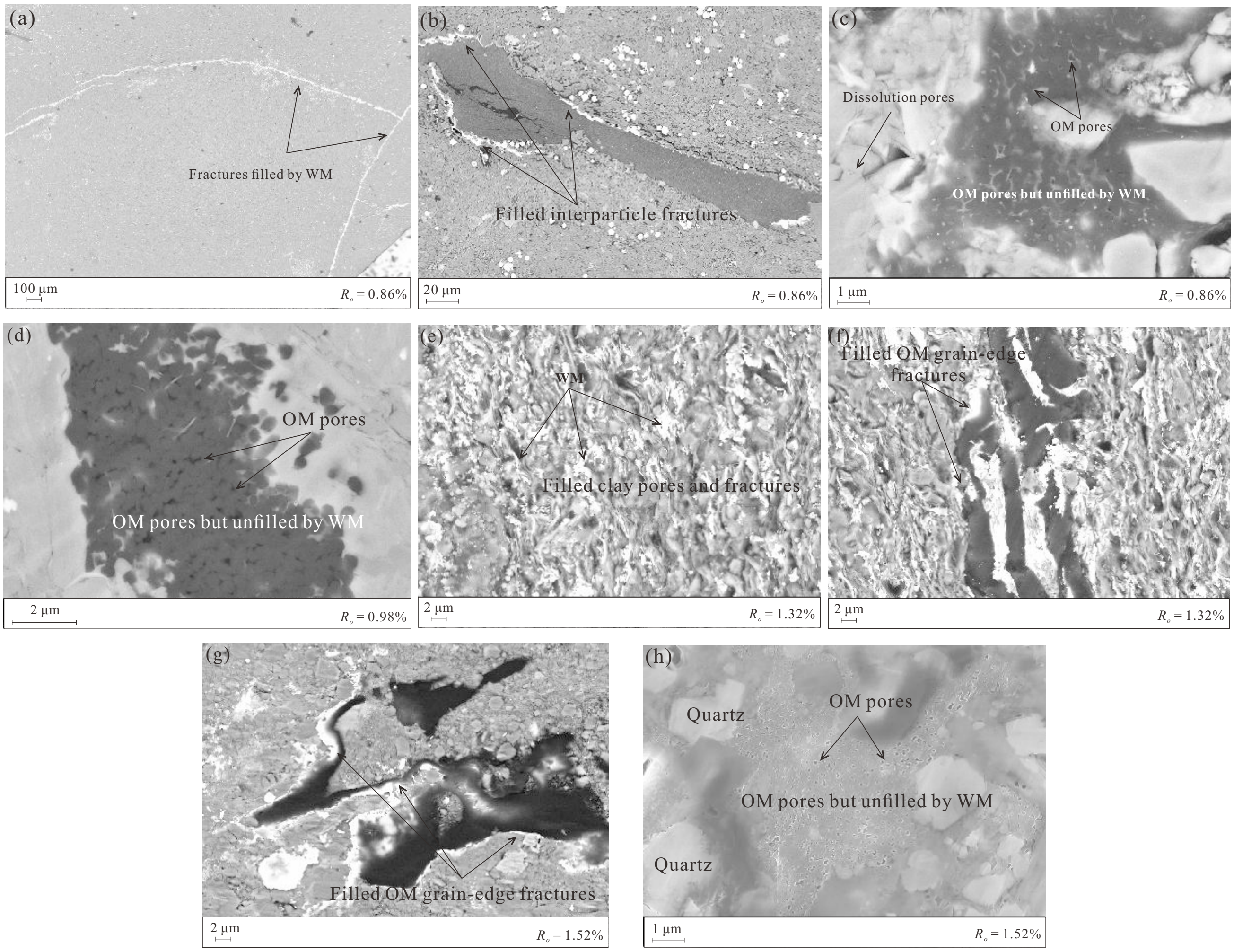

Fig. 3. FE-SEM images of mature shale samples after WM impregnation showing improved connectivity between fractures, interparticle pores and clay-related pores, but with the persistent isolation of most organic-matter pores. (a) WM-filled fractures and connected interparticle pores at 200 MPa; (b) WM in grain-edge fractures around OM but not in organic pores; (c)-(d) Organic pores and dissolution pores in adjacent minerals that remain unfilled by WM; (e)-(f) WM in clay-associated pores and fractures and along organic-matter-mineral boundaries; (g) WM occupies fractures along organic-matter–grain boundaries but is absent from the organic pores; and (h) abundant circular organic pores that are not filled by WM. (a-c) Sample C, (d) Sample D, (e)-(f) Sample E, and (g)-(h) Sample F.

phologies concentrated near bedding-parallel fractures. Despite their extensive spatial reach, most fractures are isolated and show weak linkage to matrix pores, indicating poor pore-fracture connectivity. Quantitatively, connected porosity is low (1.27-1.97%), with pore diameters of 1-30.7 μm (mean 3.24 μm).

The pore network model (PNM) indicates overall low connectivity in the shale samples (Fig. 5). The interconnected pore space is simplified into idealized elements, with spheres representing pores and cylinders representing pore throats (Fig. 5). In general, the connected domain is dominated by fractures and fracture-linked intergranular pores. Among the samples, F shows the highest connectivity, whereas sample D exhibits the lowest. As shown in Figs. S6(b), S6(d), S6(f), S6(h), S6(j), and S6(l), PNM pore diameters are < 500 μm, with a pronounced peak at 30-50 μm. Throat diameters span 10-100 μm, and most fall within 10-20 μm (Figs. S6(a), S6(c), S6(e), S6(g), S6(i), and S6(k)). Notably, sample D lacks throats in the 50-100 μm interval, whereas sample F contains the largest number of throats within this range.

4. Discussion

4.1 Pore evolution mechanisms during thermal maturity

Thermal maturity and diagenesis are widely recognized as primary controls on shale microstructure and pore development, thereby shaping the evolution of pore architecture (Mastalerz et al., 2013; Wu et al., 2019; Cao et al., 2022). Previous studies have reported weak or absent correlations between total pore volume (TPV) and TOC, suggesting that bedding fractures and inorganic pore domains can be key

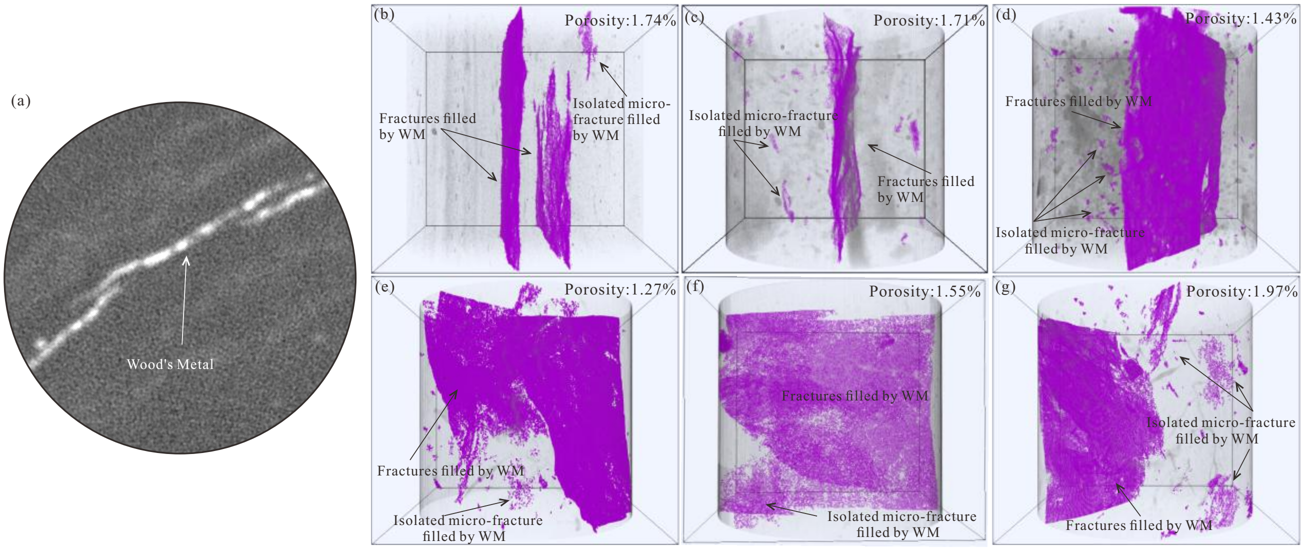

Fig. 4. CT images and 3D renderings of WM-filled fractures in lacustrine shale samples, highlighting the evolution of fracture connectivity with thermal maturity. (a) Representative CT slice showing bright WM-filled fractures; and (b)-(g) 3D fracture networks for samples A-F, respectively, where the colors denote WM-filled fracture segments. Fractures are mostly isolated and stratified in low- to middle-maturity samples, whereas sample F displays a more connected fracture network. (b) Sample A, (c) Sample B, (d) Sample C, (e) Sample D, (f) Sample E and (g) Sample F.

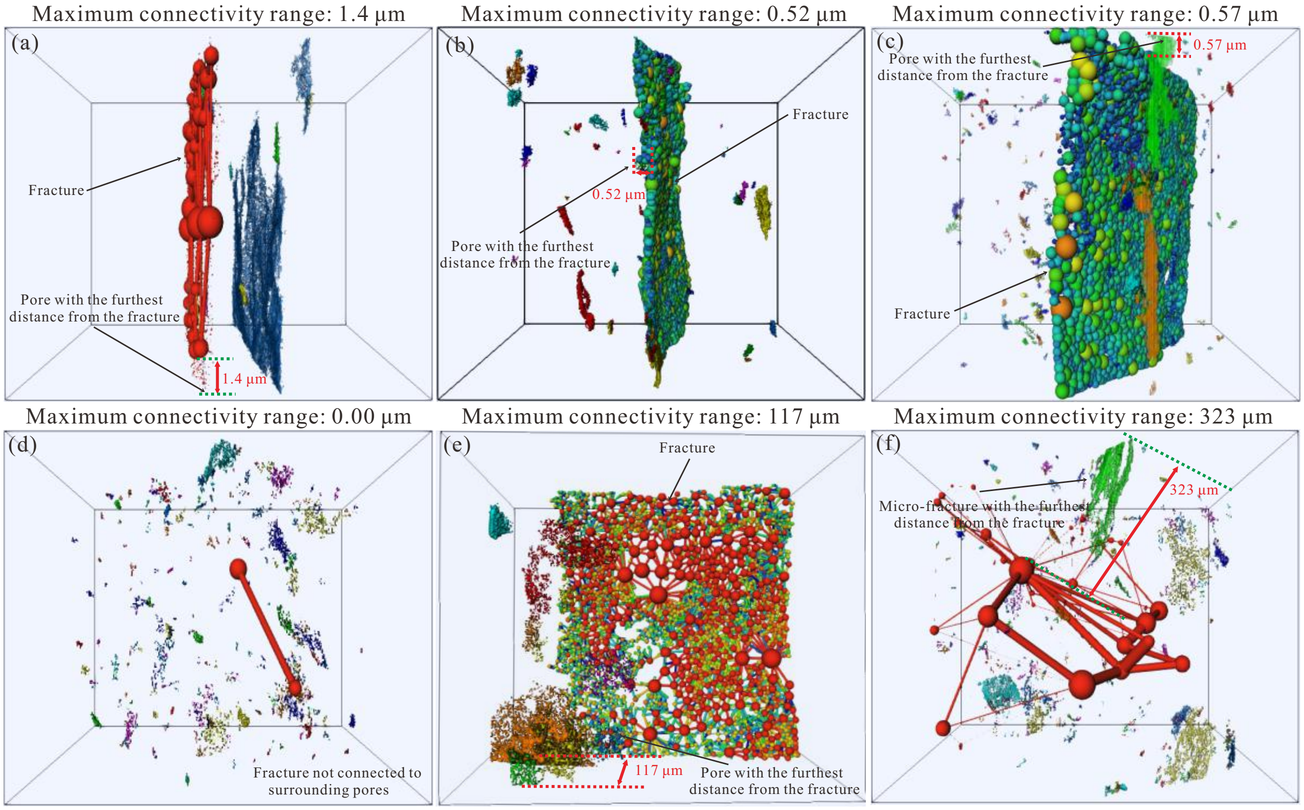

Fig. 5. Pore network models of the WM-impregnated lacustrine shale samples, illustrating the limited connectivity of the pore-throat system, where colors denote pore and throat size, spheres represent pores, and cylinders represent throats. The models show that connected pores are mainly fractures and intergranular pores linked to fractures, with sample F having the highest number of large throats and sample D having the poorest connectivity. (a) Sample A, (b) Sample B, (c) Sample C, (d) Sample D, (e) Sample E and (f) Sample F.

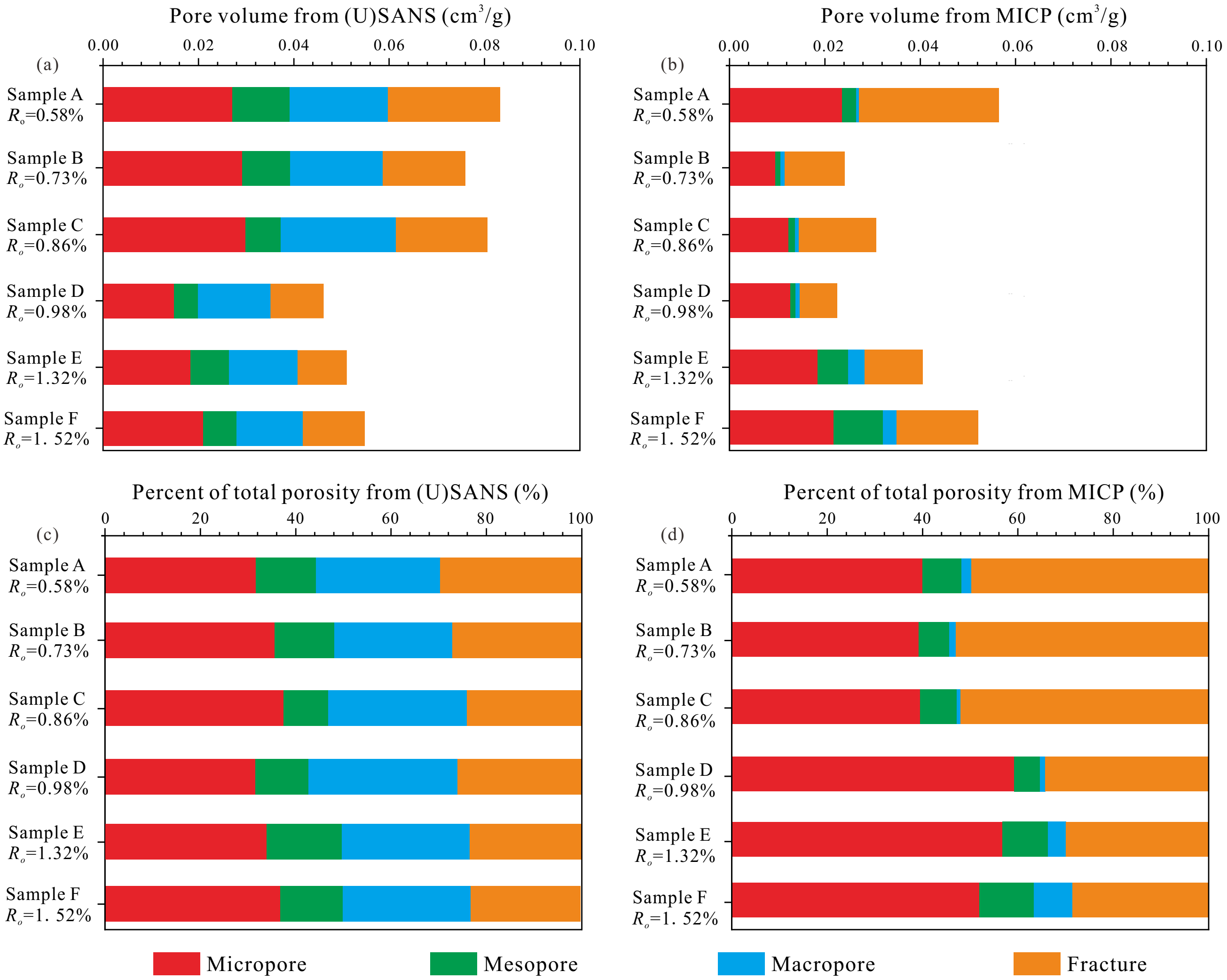

Fig. 6. (a)-(b) Volume fraction of pore-fracture system in different sizes of six shale samples from MICP and (U)SANS; (c-d) Percentages of micropores, mesopores, macropores, and fractures with increasing maturity based on the MICP and (U)SANS.

contributors to the pore-fracture system in lacustrine shales (Mastalerz et al., 2013; Xu et al., 2023). However, in shale samples of this study, no meaningful correlation was found between TOC and TPV (Fig. S7). This lack of correlation suggests that abundant shale bedding fractures and inorganic pores (e.g., intragranular pores, intergranular pores, microfractures) are key contributors to the pore-fracture system in shale (Wei et al., 2023). This observation is consistent with our FE-SEM images, where intergranular pores are predominant in shale (Figs. 2(b) and 2(c)), and many intergranular pores remain in mature shale samples (Figs. 3(b) and 3(e)). The 3D pore networks reconstructed from micro-CT scans further reveal pervasive microfractures across the shale samples (Fig. 4). Mineral composition may also influence the complexity of pore evolution as maturity progresses (Chang et al., 2022). However, in this study, no significant relationship ($R^2 > 0.5$) was identified between TPV and the clay, carbonate, quartz, or feldspar contents of the samples (Fig. S(8)). Although prior studies have reported links between mineral composition and TPV, such relationships are most often identified in shale datasets with only minor maturity contrasts, where samples cluster within a narrow maturity window, unlike the broad maturity span investigated herein (Gao et al., 2019). Overall, shale pore-structure evolution is governed by multiple factors; in our dataset, thermal maturity exerts a stronger control than TOC, burial depth or mineral composition. It should also be noted that only a single sample was analyzed for each maturity stage; therefore, the observed trends are best regarded as representative of this maturity path in the shale rather than as a statistical population.

Thermal maturity-driven pore evolution was further evaluated by quantifying pore-volume changes across representative pore-size intervals and fracture contributions. As shown in Fig. 6, pore volumes in four size bins (< 20 nm, 20-100 nm, 100-800 nm, and > 800 nm) vary systematically along the thermal-maturity sequence. Among these bins, micropores exhibit the largest variability: the neutron-scattering-derived micropore volume follows an increase-decrease-increase trend (Figs. 6(a) and 6(c)), reflecting the changes occurring within the OM. The thermal transformation of OM increases micropore volume;

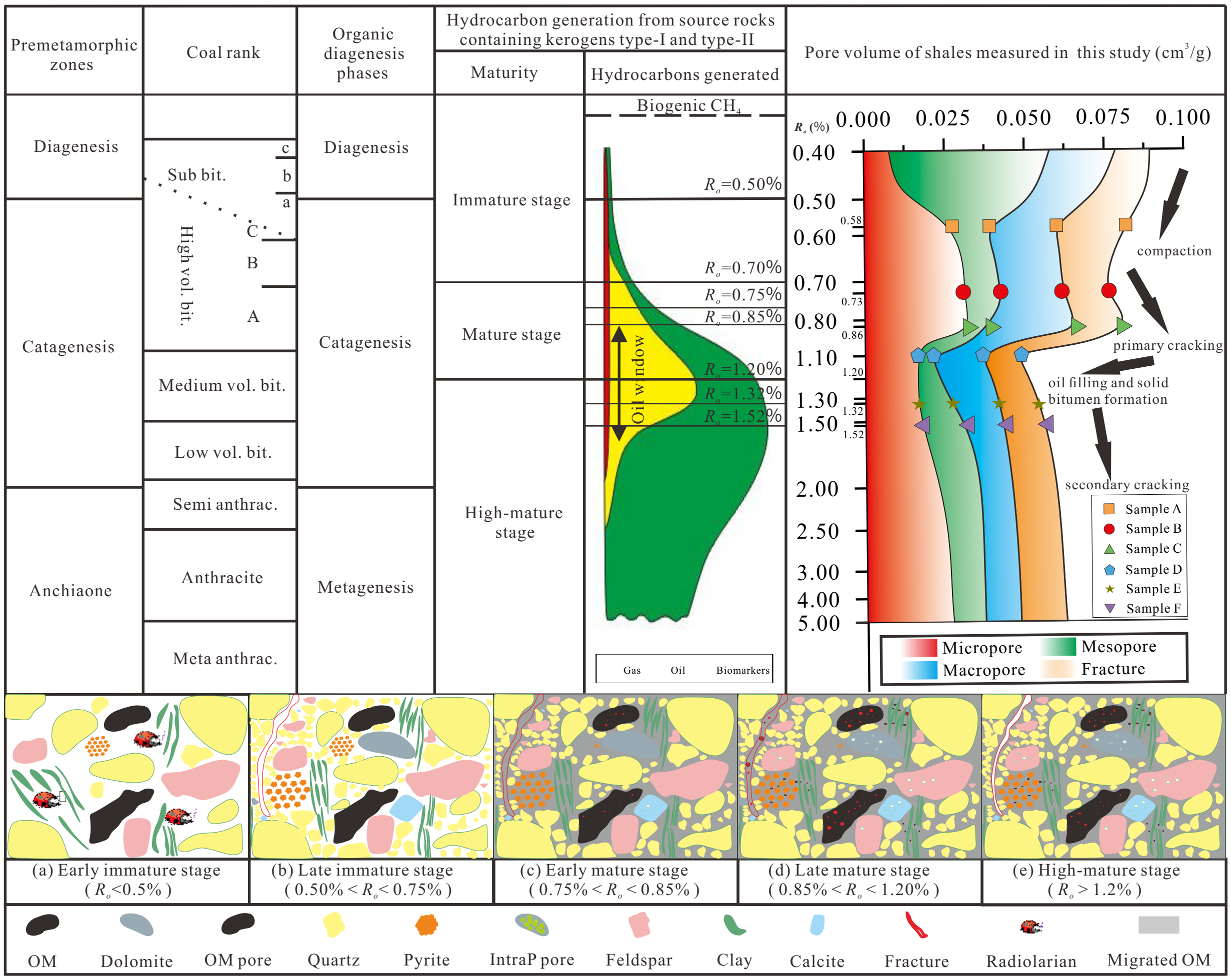

Fig. 7. Pore evolution model based on thermal maturity, diagenesis, and hydrocarbon generation. The shapes on the TPV curve indicate the positions of the samples in this study. (a)-(e) Conceptual model of diagenetic pathway and shale pore evolution associated with shale composition.

however, increasing burial depth inhibits further development of these micropores. To be more specific, when the pore pressure is less than the overburden, the volume of micropores is expected to decrease. Conversely, when the pore pressure exceeds the overburden, this trend is reversed. The volume of mesopores decreases with the progression of thermal maturity to $R_o = 0.98\%$ and then increases significantly. In this respect, studies have shown that compaction, cementation, and the infill of liquid hydrocarbon would decrease the mesopore volume (Cao et al., 2022). The subsequent increase in mesopore volume is mainly attributed to gas generation via the secondary cracking of oil and bitumen, coupled with the displacement/expulsion of residual liquid hydrocarbons (Mastalerz et al., 2013). Moreover, the overall percentage of macropores decreases with increasing maturity (Fig. 6(c)). Increased burial depth and continued compaction during diagenesis will result in a continuous reduction in macropores (Ko et al., 2018). Similar patterns of pore evolution have been observed in the Da'anzhai shale and the New Albany Shale (Gao et al., 2021). However, unlike marine shales, lacustrine shales generally exhibit major fracture development, making the evolution mode of fractures within such geologic formations equally important. The pore volume and the percentage of fractures decreased with increasing thermal progression (Figs. 6(b) and 6(d)). Fractures in terrestrial-phase shale layers are known to form during deposition; however, with an increasing depth of burial and ongoing compaction as a result, during diagenesis, these fractures gradually may close. Consequently, both the pore volume and the percentage of such pores showed steady decrease in our samples. Overall, the TPV exhibited a U-shaped response to maturity (decrease followed by recovery), with a change range of 0.58% to 1.52% (Figs. 6(b) and 6(d)). This variation is highly attributed to the thermal maturation and diagenesis of lacustrine shale (Zhang et al., 2021; Wang et al., 2022).

This study proposes a pore-evolution model for lacustrine shale based on previous research across a range of thermal maturities (Fig. 7).

This conceptual model summarizes prior work across a wide thermal-maturity spectrum (Fig. 7) and integrates hydrocarbon generation, diagenetic modification, and thermal maturation (Cao et al., 2022) to describe pore development

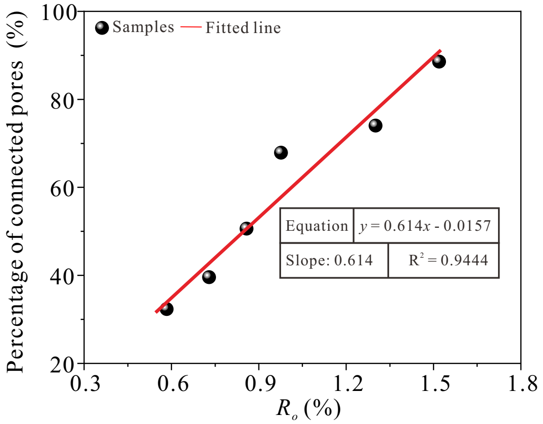

Fig. 8. Relationship between 1st MICP / (U)SANS porosity (3-30 nm) of shales with different thermal maturities.

in complex shale formations. The maturity trajectory according to thermal progression is classified into five stages: early immature ($R_o < 0.5\%$), late immature ($0.5\% < R_o < 0.75\%$), early mature ($0.75\% < R_o < 0.85\%$), late mature ($0.85\% < R_o < 1.2\%$), and high-maturity ($R_o > 1.2\%$) (Fig. 7). At the early immature stage, sediments consist primarily of bioclasts, minerals, and semi-consolidated or unconsolidated loose particles (Fig. 7(a)). The pore space is dominated by intergranular pores, fractures and mineral grains. At this stage, total porosity is high due to minimal compaction from the low overburden, explaining the largest TPV observed in our lowest maturity shale sample, A ($R_o = 0.58\%$) (Table 1). As burial depth and compaction increase, pore space diminishes, potentially being filled by cement, mud or calcite (Lai et al., 2017). Intergranular pores remain dominant, while OM pores are undeveloped (Fig. 2). As a result, TPV continues to decrease during the late immature stage (Fig. 7(b)). In early maturity stage, OM pores begin to develop with irregular shapes as solid OM is converted into liquid hydrocarbons and associated gases (Fig. 7(c)). Several studies have reported that pores with sizes of 2-50 nm increase in abundance as solid kerogen is transformed into petroleum (Wu et al., 2019; Gao et al., 2021). However, the FE-SEM and (U)SANS results show that organic pores smaller than 20 nm are primarily developed at this stage (Figs. S5(b) and 5(c)), while pore volume between 20 and 50 nm decreases in our samples (Fig. S5(b), Table S2). In addition, dissolution pores were identified in sample C (Fig. 3(c)), which are likely produced by the dissolution of unstable minerals (feldspar and calcite) driven by interaction with organic acids after liquid-hydrocarbon expulsion (Cao et al., 2022). At the late maturity stage, large quantities of liquid hydrocarbons fill both organic and inorganic pores (intergranular, intragranular pores, and fractures connected to OM) (Fig. 7(d)), causing a dramatic reduction in TPV. Strong compaction and cementation further reduce TPV during this stage (Wang et al., 2021a; Cao et al., 2022). At high maturity, the secondary cracking of liquid hydrocarbons into gas begins (Fig. 7(e)) and OM pores continue to develop, forming sponge-like pores with enhanced connectivity (Fig. 3(h)). The ongoing transformation of liquid hydrocarbons into stable gaseous hydrocarbons increases pore pressure within organic pores, mitigating pore closure or deformation as burial depth increases (Yang et al., 2016). As a result, TPV significantly increases during this stage.

4.2 Pore-fracture connectivity during thermal maturity progression

Pore-fracture network connectivity in shale plays a key role as a controlling factor influencing shale oil transportation and production (Hu et al., 2015; Sun et al., 2023). Shale pore-fracture network connectivity encompasses both the interconnectivity among matrix pores and that between network of fractures and matrix pores (Sun et al., 2022, 2023). Studies of pore connectivity in the Barnett Shale have documented that high matrix pore connectivity and poor matrix pore-fracture connectivity favor hydrocarbon storage (Hu et al., 2015). Conversely, reservoirs exhibiting both high matrix pore connectivity and high matrix pore-fracture connectivity tend to have high initial production rates. However, these reservoirs often experience rapid production decline, ultimately impacting the overall recovery rates (Sigal, 2013). Given the complex nature of pore system connectivity within shale, this study conducted a comprehensive analysis of shale pore connectivity across different maturity levels. This was achieved by combining repeat MICP, FE-SEM imaging after WM impregnation, and CT measurements following WM injection.

Matrix-pore connectivity can be evaluated through MICP and (U)SANS measurements. The porosity obtained by the MICP represents the porosity of the connected pore, whereas the porosity detected by (U)SANS accounts for the porosity of the TPV. Therefore, the percentage of connected pores can be calculated by Eq. (4). An increase in the first MICP/(U)SANS ratio with thermal maturity indicates that a larger fraction of nanopores becomes connected through effective pore throats:

$$\eta = \frac{\rho_M}{\rho_S} \tag{4}$$

where η represents the percentage of connected pores; ρ_M represents the MICP porosity in the range of 3-30 nm; ρ_S is the (U)SANS porosity in the range of 3-30 nm.

To clarify how maturation influences the connected pore network in these shale samples, matrix pore connectivity was further examined in relation to thermal maturity. Fig. 8 illustrates the linkage between thermal maturity and the fraction of connected pores in the shale samples. With increasing thermal maturity, the fraction of the 1st MICP/(U)SANS porosity (3-30 nm) gradually increases, indicating that matrix pore connectivity within the OM improves as shale matures. Sun et al. (2020) used FIB-SEM-based 3D pore-network reconstruction in a mature marine shale sample and found that matrix pores within the OM generally exhibited good connectivity, which aligns with the findings of this study. Furthermore, FE-SEM imaging after WM impregnation showed that the most mature sample, F, had the highest connectivity, evidenced by the greatest amount of WM present in the matrix pores (Fig. 4(g)). Therefore, increased thermal maturity promotes the development of organic pores, enhancing matrix pore connectivity in shale. Moreover, the rigid framework formed by brittle minerals (e.g., quartz, feldspar) resists compression, preventing the destruction of organic pores during diagenesis

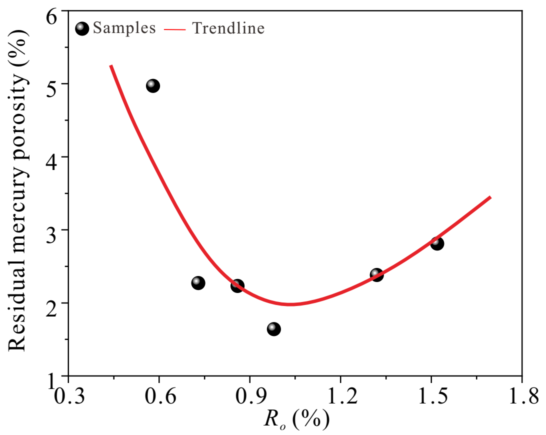

Fig. 9. Relationship between the residual mercury porosity and R_o of shales.

and ensuring increased matrix pore connectivity as shale matures.

Repeated-MICP measurements can provide us with pore spaces that are more accessible to mercury, thus enabling the quantitative assessment of pore-fracture connectivity between matrix pores and fractures in the samples (Yu et al., 2019). Repeated-MICP experiments reveal a non-linear trend in residual mercury porosity. As maturity increases, the residual porosity first decreases and later increases (Fig. 9). The residual mercury porosity serves as a quantitative indicator of the pore-fracture connectivity, i.e., that between pores and fractures within shale (Zhao et al., 2023). Therefore, this trend further indicates that matrix-fracture connectivity initially declines and subsequently increases with increasing thermal maturity. The initial decrease in residual mercury is mainly attributed to fracture closure and liquid hydrocarbon filling during compaction, whereas the subsequent increase is interpreted to reflect the partial reopening of fractures associated with secondary gas generation at high maturity. Moreover, FE-SEM images of the specimens after WM injection at 200 MPa present a better filling of matrix pores with WM along the fractures with increased maturity (Figs. 2 and 3). This infers that thermal maturity improves pore connectivity between matrix pores and fractures in shale samples. It is worth noting that the WM-filled organic pores were not observed in the FE-SEM images, which disagrees with the intrusion volume in the pore-throat measured by the MICP (3-20 nm pores) (Fig. S3(b)). There are two possible reasons for this contradiction: (1) the limitation in the SEM field of view fails to observe WM-filled organic pores (Fan et al., 2022); (2) Sun et al. (2023) further demonstrated that the elastic straining of the matrix, together with the plastic deformation of pores, can enhance pore-throat intrusion in the 3-20 nm size range. In addition, CT measurements following WM impregnation also confirmed that as maturity increases, the connectivity between fractures and surrounding matrix pores first decreased and then increased. This variation is closely linked to the generation and expulsion of liquid hydrocarbon compounds in organic-rich shale. Specifically, the fractures within D shale sample exhibited the poorest connectivity with the surrounding matrix pores (Fig. 5(d)) which is in the liquid hydrocarbon expulsion stage (Fig. 7). In contrast, shale sample F, which is in the stage of secondary liquid hydrocarbon cracking into gas, exhibited strong connectivity between fractures and the surrounding matrix pores (Figs. 5(f) and 6).

Residual mercury in different pore systems, measured by repeated-MICP, varies significantly with increasing maturity, reflecting the connectivity of each pore system (Fig. 1). Overall, both pores smaller than 20 nm and those larger than 800 nm exhibited a decreasing trend in residual mercury with increasing maturity (Fig. 1). In contrast, a gradual increase was observed in pores ranging from 20 to 100 nm (Fig. 1). This change may be attributed to processes associated with hydrocarbon generation and diagenesis (Mastalerz et al., 2013; Cao et al., 2022). The 3D network reconstructions from FIB-SEM images indicate that the widespread development of organic pores can improve the connectivity of pores smaller than 20 nm (Sun et al., 2020). However, intergranular and intragranular pores (20-100 nm), often filled with expelled liquid hydrocarbons, tend to increase the number of closed pores (Mastalerz et al., 2013). Interestingly, the overall deterioration of pore connectivity observed in samples with varying thermal maturities was alleviated by the secondary cracking of liquid hydrocarbons. In this study, the F shale sample showed a significantly reduced amount of residual mercury in the 20-100 nm pores (Fig. 1). Taken together, the documented pore evolution and the multi-perspective analyses presented here provide a valuable basis for guiding future exploitations of continental shale reservoirs that span a broad range of thermal maturities worldwide.

4.3 CO_2 storage potential of shales with different maturity levels

Lacustrine shale reservoirs, which are characterized by abundant nanopores and high SSA, are important targets for CO_2 geological storage. Shales not only act as regional caprocks but can also serve as storage formations in which CO_2 is immobilized predominantly by adsorption and capillary trapping (Glatz et al., 2022; Zhou et al., 2025). The (U)SANS results of this study indicate that the total SSA of the shale varies from 17.39 to 26.93 m^2/g, and the maximum value (26.93 m^2/g) occurs in the high-maturity sample F (Table 2). Micropores contribute 10.26–15.13 m^2/g at middle maturity and increase to 18.31 m^2/g at high maturity (Table 2), indicating that mature to high-mature shales provide more pore surface area and a greater number of potential sorption sites for CO_2 than low-maturity shales. However, the complex evolution of the pore–fracture system during thermal maturation, in conjunction with hydrocarbon generation and expulsion, can significantly influence the long-term CO_2 storage performance (Li et al., 2024). Most CO_2 storage and CO_2-EOR operations are conducted in high-maturity shales (Wang et al., 2023). However, our results indicate that mature shales also provide favorable CO_2 storage conditions: their abundant organic pores and the expulsion of liquid hydrocarbons create large pore space and high surface area for CO_2 adsorption (Fig. 3; Table 2). In addition, abundant carbonate minerals in mature shales readily react with CO_2 to form stable carbonate compounds, enhancing sealing stability. As a result, mature shales exhibit greater potential for long-term CO_2 storage than high-maturity shales.

Besides the abundant organic pores and high SSA in mature shale, long-term CO_2 storage is also affected by changes in pore connectivity due to thermal maturation. Enhanced nanoscale organic pore connectivity in mature shales (Figs. 7 and 9) improves matrix quality (Glatz et al., 2022), facilitating efficient CO_2 storage. At the same time, the CO_2 injection can reduce the viscosity of liquid hydrocarbons and enhance shale oil recovery (Huang et al., 2023). Repeated-MICP and CT scanning indicate an overall reduction in pore connectivity in mature shale (Figs. 6 and 8), primarily due to strong compaction and hydrocarbon drainage, which helps to mitigate CO_2 leakage (Geng et al., 2017). Furthermore, stable carbonate minerals formed by reactions between CO_2 and carbonate minerals lower the thermal expansion coefficient of the minerals, inhibit fracture growth, and contribute to long-term CO_2 storage stability (Cao et al., 2020; Sun et al., 2025). Overall, the degree of thermal maturation, hydrocarbon generation and expulsion, pore connectivity, and fracture propagation jointly control the long-term stability of CO_2 storage, and our integrated results suggest that mature to high-maturity shales with well-developed nanopores and reduced fracture connectivity are more favorable for long-term CO_2 storage than overmature shales with reactivated fracture networks.

5. Conclusions

In this work, the pore-fracture system evolution and its connectivity in lacustrine shale (R_o 0.58%-1.52%) were investigated using repeated-MICP, (U)SANS, FE-SEM after WM impregnation, and micro-CT scanning. Thermal maturity is the primary control on pore-fracture architecture and connectivity, and therefore on long-term CO_2 storage capacity.

1) According to the fractal characteristics and inflection points of the MICP curves, the pore system is divided into four pore-size classes: micropores (< 20 nm), mesopores (20-100 nm), macropores (100-800 nm) and fractures (> 0.8 μm).
2) The combined MICP and (U)SANS results show that the relative contributions of these four pore-size classes evolve systematically with increasing maturity. Mechanical compaction and early cementation preferentially reduce macropores and fractures, whereas organic matter-hosted micropores become increasingly important at high maturity.
3) The TPV exhibits a non-linear evolution with thermal maturity: It slightly increases at early maturity, decreases at intermediate maturity when compaction and liquid hydrocarbons occupy part of the pore space, and increases again at high maturity due to secondary gas generation and the partial reopening of previously closed pores and fractures.
4) Repeated-MICP, CT scanning and FE-SEM observations after WM impregnation reveal that connectivity between matrix pores and fracture networks initially decreases and subsequently increases with increasing maturity. Hydrocarbon generation and diagenetic processes initially reduce pore and fracture connectivity, whereas the secondary cracking of liquid hydrocarbons reopens blocked pores and enhances overall connectivity at high maturity.
5) Abundant organic pores in mature shales provide effective space for CO_2 storage, and the reduced connectivity caused by compaction and liquid hydrocarbons helps limit CO_2 leakage. In contrast, the increased pore connectivity in overmature shales is less favorable for long-term CO_2 sequestration.

Acknowledgements

The authors sincerely thank the National Natural Science Foundation (Nos. 42272159 and U23A20596) and the Superior Youth Foundation of Heilongjiang Province (No. YQ2023D002) of China for their financial support. We gratefully acknowledge ANSTO for providing beamtime and extend our thanks to Liliana de Campo and Chunming Wu for their assistance in analyzing the neutron scattering data.

Supplementary file

https://doi.org/10.46690/ager.2026.01.07

Conflicts of interest

The authors declare no competing interest.

References

Cao, C., Liu, H., Hou, Z., et al. A review of CO_2 storage in view of safety and cost-effectiveness. Energies, 2020, 13(3): 600.

Cao, T., Liu, H., Pan, A., et al. Pore evolution in siliceous shales and its influence on shale gas-bearing capacity in eastern Sichuan-western Hubei, China. Journal of Petroleum Science and Engineering, 2022, 208: 109597.

Chang, J., Fan, X., Jiang, Z., et al. Differential impact of clay minerals and organic matter on pore structure and its fractal characteristics of marine and continental shales in China. Applied Clay Science, 2022, 216: 106334.

Fan, Y., Liu, K., Yu, L., et al. Assessment of multi-scale pore structures and pore connectivity domains of marine shales by fractal dimensions and correlation lengths. Fuel, 2022, 330: 125463.

Gao, Z., Fan, Y., Hu, Q., et al. A review of shale wettability characterization using spontaneous imbibition experiments. Marine and Petroleum Geology, 2019, 109: 330-338.

Gao, Z., Xuan, Q., Hu, Q., et al. Pore structure evolution characteristics of continental shale in China as indicated from thermal simulation experiments. AAPG Bulletin, 2021, 105(11): 2159-2180.

Geng, Y., Liang, W., Liu, J., et al. Evolution of pore and fracture structure of oil shale under high temperature and high pressure. Energy & Fuels, 2017, 31(10): 10404-

10413.

Glatz, G., Alafnan, S., Gholami, R., et al. Effect of kerogen maturity on the adsorption capacity of CO_2 and CH_4: A molecular investigation. Fuel, 2022, 327: 125188.

Hua, G., Wu, S., Zhang, J., et al. Laminar structure and reservoir quality of shales with high clay mineral content in the qingshankou formation, songliao basin. Energies, 2022, 15(17): 6132.

Huang, X., Tian, Z., Zuo, X., et al. The microscopic pore crude oil production characteristics and influencing factors by DME-assisted CO_2 injection in shale oil reservoirs. Fuel, 2023, 331: 125843.

Hu, Q., Ewing, R. P., Rowe, H. D. Low nanopore connectivity limits gas production in Barnett formation. Journal of Geophysical Research: Solid Earth, 2015, 120(12): 8073-8087.

Jarvie, D. M. Geochemical assessment and characterization of petroleum source rocks and oils, and petroleum systems. The Houston Geological Society Bulletin, 2017, 60(4): 14-18.

Jarvie, D. M., Hill, R. J., Ruble, T. E., et al. Unconventional shale-gas systems: The Mississippian Barnett Shale of north-central Texas as one model for thermogenic shale-gas assessment. AAPG Bulletin, 2007, 91(4): 475-499.

Ko, L. T., Ruppel, S. C., Loucks, R. G., et al. Pore-types and pore-network evolution in Upper Devonian-Lower Mississippian Woodford and Mississippian Barnett mudstones: Insights from laboratory thermal maturation and organic petrology. International Journal of Coal Geology, 2018, 190: 3-28.

Lai, J., Wang, G., Chai, Y., et al. Deep burial diagenesis and reservoir quality evolution of high-temperature, high-pressure sandstones: Examples from Lower Cretaceous Bashijiqike Formation in Keshen area, Kuqa depression, Tarim basin of China. AAPG Bulletin, 2017, 101(6): 829-862.

Li, A., Ding, W., He, J., et al. Investigation of pore structure and fractal characteristics of organic-rich shale reservoirs: A case study of Lower Cambrian Qiongzhusi formation in Malong block of eastern Yunnan Province, South China. Marine and Petroleum Geology, 2016, 70: 46-57.

Li, L., Zhang, D., Su, Y., et al. Microfluidic insights into CO_2 sequestration and enhanced oil recovery in laminated shale reservoirs: Post-fracturing interface dynamics and micro-scale mechanisms. Advances in Geo-Energy Research, 2024, 13(3): 203-217.

Liu, B., Mohammadi, M. R., Ma, Z., et al. Evolution of porosity in kerogen type I during hydrous and anhydrous pyrolysis: Experimental study, mechanistic understanding, and model development. Fuel, 2023, 338: 127149.

Liu, K., Ostadhassan, M., Zhou, J., et al. Nanoscale pore structure characterization of the Bakken shale in the USA. Fuel, 2017, 209: 567-578.

Loucks, R. G., Reed, R. M., Ruppel, S. C., et al. Spectrum of pore types and networks in mudrocks and a descriptive classification for matrix-related mudrock pores. AAPG Bulletin, 2012, 96(6): 1071-1098.

Mastalerz, M., Schimmelmann, A., Drobniak, A., et al. Porosity of Devonian and Mississippian New Albany Shale across a maturation gradient: Insights from organic petrology, gas adsorption, and mercury intrusion. AAPG Bulletin, 2013, 97(10): 1621-1643.

Sigal, R. Mercury capillary pressure measurements on Barnett core. SPE Reservoir Evaluation & Engineering, 2013, 16(04): 432-442.

Sun, L., Liu, H., He, W., et al. An analysis of major scientific problems and research paths of Gulong shale oil in Daqing Oilfield, NE China. Petroleum Exploration and Development, 2021, 48(3): 527-540.

Sun, L., Wang, H., Li, G., et al. Micromechanical damage and proppant embedment patterns of fracture surfaces in lacustrine shale CO_2 pre-pad energized fracturing. Petroleum Exploration and Development, 2025, 52(4): 1041-1052.

Sun, M., Duan, X., Liu, Q., et al. The importance of pore-fracture connectivity in overmature marine shale for methane occurrence and transportation. Marine and Petroleum Geology, 2023, 157: 106495.

Sun, M., Wen, J., Pan, Z., et al. Pore accessibility by wettable fluids in overmature marine shales of China: Investigations from contrast-matching small-angle neutron scattering (CM-SANS). International Journal of Coal Geology, 2022, 255: 103987.

Sun, M., Zhao, J., Pan, Z., et al. Pore characterization of shales: A review of small angle scattering technique. Journal of Natural Gas Science and Engineering, 2020, 78: 103294.

Wang, Y., Cheng, H., Hu, Q., et al. Diagenesis and pore evolution for various lithofacies of the Wufeng-Longmaxi shale, southern Sichuan Basin, China. Marine and Petroleum Geology, 2021a, 133: 105251.

Wang, X., Wang, M., Li, J., et al. Thermal maturity: The controlling factor of wettability, pore structure, and oil content in the lacustrine Qingshankou shale, Songliao Basin. Journal of Petroleum Science and Engineering, 2022, 215: 110618.

Wang, L., Yang, H., Guo, Y., et al. Comparative study of marine and lacustrine shale reservoirs from the viewpoint of rock mechanics. Energy & Fuels, 2021b, 35(23): 19481-19495.

Wang, L., Zhang, Y., Zou, R., et al. A systematic review of CO_2 injection for enhanced oil recovery and carbon storage in shale reservoirs. International Journal of Hydrogen Energy, 2023, 48(95): 37134-37165.

Wei, J., Zhang, A., Li, J., et al. Study on microscale pore structure and bedding fracture characteristics of shale oil reservoir. Energy, 2023, 278: 127829.

Wei, M., Zhang, L., Xiong, Y., et al. Main factors influencing the development of nanopores in over-mature, organic-rich shales. International Journal of Coal Geology, 2019, 212: 103233.

Wen, J., Sun, M., Cui, Z., et al. Characterization of crude oil charging of Xiaoerbulake dolomite in the Tarim basin: Insights from bitumen distribution. Marine and Petroleum Geology, 2023, 148: 106023.

Wen, J., Yu, B., Ji, Y., et al. Controls of anisotropy and pore connectivity on gas retainment and flow in deep shale of Longmaxi Formation. Discover Geoscience, 2025, 3(1): 202.

Wu, S., Yang, Z., Zhai, X., et al. An experimental study of organic matter, minerals and porosity evolution in shales within high-temperature and high-pressure constraints. Marine and Petroleum Geology, 2019, 102: 377-390.

Xu, L., Pan, R., Hu, H., Meng, J. Contribution of various shale components to pore system: Insights from attributes analysis. Journal of Marine Science and Engineering, 2023, 11(7): 1327.

Yang, R., He, S., Yi, J., et al. Nano-scale pore structure and fractal dimension of organic-rich Wufeng-Longmaxi shale from Jiaoshiba area, Sichuan Basin: Investigations using FE-SEM, gas adsorption and helium pycnometry. Marine and Petroleum Geology, 2016, 70: 27-45.

Yu, Y., Luo, X., Wang, Z., et al. A new correction method for mercury injection capillary pressure (MICP) to characterize the pore structure of shale. Journal of Natural Gas Science and Engineering, 2019, 68: 102896.

Zhang, P., Misch, D., Hu, F., et al. Porosity evolution in organic matter-rich shales (Qingshankou Fm.; Songliao Basin, NE China): Implications for shale oil retention. Marine and Petroleum Geology, 2021, 130: 105139.

Zhao, X., Sun, M., Ukaomah, C. F., et al. Pore connectivity and microfracture characteristics of Longmaxi shale in the Fuling gas field: Insights from mercury intrusion capillary pressure analysis. Gas Science and Engineering, 2023, 119: 205134.

Zhao, Z., Littke, R., Zieger, L., et al. Depositional environment, thermal maturity and shale oil potential of the Cretaceous Qingshankou Formation in the eastern Changling Sag, Songliao Basin, China: An integrated organic and inorganic geochemistry approach. International Journal of Coal Geology, 2020, 232: 103621.

Zhou, H., Wang, B., Zhou, F. Mechanical, structural, and mineralogical changes of shale under acid-CO_2-rock interactions and their implications for CO_2 storage. Petroleum Science, 2025.